CARM Amplifier Theory
and Simulation

Chen, C.; Danly, B.G.; Davies, J.A.[†];

Menninger, W.L.; Wurtele, J.S.; Zhang, G.[†]

Plasma Fusion Center

Massachusetts Institute of Technology

Cambridge, MA 02139

September 1990

[†] Permanent Address: Department of Physics, Clark University, Worcester, MA

ABSTRACT

The theory and simulation of cyclotron autoresonance maser (CARM) amplifiers are presented, including studies of amplifier phase stability, multimode phenomena, and susceptibility to absolute instabilities. Recent results include particle-in-cell simulations of the onset of absolute instabilities and numerical modeling of multimode effects. Phase stability studies indicate that the output phase of CARM amplifiers may be relatively insensitive to fluctuations in beam energy, pitch, and current, for optimized designs; simulations show a phase sensitivity of $\sim 2°$ per percent beam energy variation. An experimental design for a long-pulse 17 GHz CARM amplifier is presented.

1

1. INTRODUCTION

Future linear colliders will require high frequency rf sources together with high gradient accelerating structures in order to be economically feasible. The cyclotron autoresonance maser (CARM) is a promising source for application as an rf accelerator driver, and a program to develop CARM amplifiers at 17 GHz for this application is presently underway at the MIT Plasma Fusion Center [1].

Experiments at a 17 GHz will be performed using two different technologies for generation of the high voltage electron beam required by the CARM. A long-pulse (2.5 μs, 1 μs flattop), 700 kV pulse modulator and a short-pulse (50 ns), 1.2 MeV induction accelerator will be employed for generation of the electron beam. This will allow a comparison of two alternate methods for producing the ~ 50 ns rf pulses required by the high gradient structures. A long-pulse, modulator-driven CARM together with pulse compression techniques, or an induction-linac-driven CARM are both capable in principle of delivering the required rf pulses to the structure.

In this paper, several theoretical issues are discussed, including the behavior of the CARM amplifier with the presence of multiple modes, particle-in-cell simulations of amplifier stability, and an analysis of phase stability in the CARM amplifier. Finally, an experimental design for a long-pulse CARM amplifier is presented.

2. MULTIMODE CARM AMPLIFIER THEORY

Many planned CARM amplifier experiments will operate in overmoded waveguide. Until now, CARM amplifiers have been analyzed under *a priori* assumption that only a single waveguide mode interacts with the electron beam. The goal of this section to develop a formalism which can treat overmoded systems with an arbitrary number of transverse-electric (TE) and transverse-magnetic (TM) modes. The present analysis consists of two approaches: (kinetic) linear theory and three-dimensional, self-consistent computer simulations. For simplicity, we present here the analysis of TE_{1n} modes coupling to an azimuthally symmetric electron beam at the fundamental cyclotron frequency, while maintaining the general features of multimode CARM interactions.

It can be shown that a complete set of nonlinear equations describing an overmoded CARM amplifier with multiple TE_{1n} modes can be expressed in the dimensionless form [2,3]

$$\frac{d\gamma}{d\hat{z}} = -\frac{\hat{p}_\perp}{\hat{p}_z} \sum_n X_n(r_L, r_g) A_n \cos\psi_n \,, \tag{1}$$

$$\frac{d\hat{p}_z}{d\hat{z}} = -\frac{\hat{p}_\perp}{\hat{p}_z} \sum_n X_n(r_L, r_g) \left[\left(\frac{1}{\beta_{\phi n}} + \frac{d\delta_n}{d\hat{z}} \right) A_n \cos\psi_n + \frac{dA_n}{d\hat{z}} \sin\psi_n \right] \,, \tag{2}$$

2

$$\frac{d\psi_n}{d\hat{z}} = \frac{1}{\beta_{\phi n}} + \frac{d\delta_n}{d\hat{z}} - \frac{\gamma}{\hat{p}_z} + \frac{\hat{\Omega}_c}{\hat{p}_z}$$

$$+ \frac{1}{\hat{p}_z \hat{p}_\perp} \sum_{n'} W_{n'}(r_L, r_g) \left\{ \left[\gamma - \hat{p}_z \left(\frac{1}{\beta_{\phi n'}} + \frac{d\delta_{n'}}{d\hat{z}} \right) \right] A_{n'} \sin \psi_{n'} + \hat{p}_z \frac{dA_{n'}}{d\hat{z}} \cos \psi_{n'} \right\}, \quad (3)$$

$$\left(\frac{d^2}{d\hat{z}^2} + \frac{1}{\beta_{\phi n}^2} \right) A_n(\hat{z}) \exp\left\{ i \left[\frac{\hat{z}}{\beta_{\phi n}} + \delta_n(\hat{z}) \right] \right\}$$

$$= \frac{2ig_n}{\beta_{\phi n}} \left\langle X_n(r_L, r_g) \frac{\hat{p}_\perp}{\hat{p}_z} e^{-i\psi_n} \right\rangle \exp\left\{ i \left[\frac{\hat{z}}{\beta_{\phi n}} + \delta_n(\hat{z}) \right] \right\}, \quad (4)$$

where the normalized coupling constant g_n is defined by

$$g_n = \frac{4(\beta_{\phi n}^2 - 1)}{\beta_{\phi n}(\nu_n^2 - 1)[J_1(\nu_n)]^2} \left(\frac{I_b}{I_A} \right). \quad (5)$$

Equations (1)-(3) describe the dynamics of each individual particle, and Eq. (4) describes the slowly varying wave amplitude $A_n(\hat{z})$ and phase shift $\delta(\hat{z})$ for the TE_{1n} mode. In Eqs. (1)-(5), $\hat{z} = \omega z/c$ is the normalized interaction length; $\omega = 2\pi f$ is the angular frequency of the input signal; $\hat{\Omega}_c = \Omega_c/\omega = eB_0/mc\omega$ is the normalized nonrelativistic cyclotron frequency; $\hat{p}_z = p_z/mc = \gamma\beta_z$, $\hat{p}_\perp = p_\perp/mc = \gamma\beta_\perp$, and $\gamma = (1 + \hat{p}_z^2 + \hat{p}_\perp^2)^{1/2}$ are, respectively, the normalized axial and transverse momentum components, and relativistic mass factor of the beam electron; I_b is the beam current; $I_A = mc^3/e \cong 17$ kA is the Alfvén current; $X_n(r_L, r_g) = J_0(k_n r_g) J_1'(k_n r_L)$ and $W_n(r_L, r_g) = J_0(k_n r_g) J_1(k_n r_L)/k_n r_L$ are geometric factors; $J_0(x)$ is the zeroth-order Bessel function; $J_1'(x) = dJ_1(x)/dx$ is the derivative of the first-order Bessel function; ν_n is the nth zero of $J_1'(x)$; $k_n = \nu_n/r_w$ is the transverse wavenumber associated with the TE_{1n} mode; $\beta_{\phi n} = \omega/ck_{zn} = (1 - c^2 k_n^2/\omega^2)^{-1/2}$ is the normalized phase velocity of the vacuum TE_{1n} waveguide mode; $r_L = p_\perp/m\Omega_c$ is the electron Larmor radius; r_g is the electron guiding-center radius which is assumed to be constant. In Eq. (4), $< \cdots >$ denotes the ensemble average over the particle distribution, and typically more than 1024 particles are used in the simulations. The rf power flow over the cross section of the waveguide for the TE_{1n} mode, $P_n(z)$, is related to the normalized wave amplitude A_n by the expression

$$P_n(\hat{z}) = \frac{1}{2g_n} \left(\frac{m^2 c^5}{e^2} \right) \left(\frac{I_b}{I_A} \right) \left(1 + \beta_{\phi n} \frac{d\delta_n}{d\hat{z}} \right) A_n^2(\hat{z}), \quad (6)$$

where $m^2 c^5/e^2 \cong 8.7$ GW.

3

By performing the Laplace transform of the linearized Maxwell-Vlasov equations, a dispersion relation and amplitude equations can be derived for the cyclotron resonance maser interaction with multiple TE_{1n} modes coupling to a cold, thin ($k_n r_g \ll 1$), azimuthally symmetric electron beam. To leading order in $c^2 k_n^2/(\omega - \Omega_c/\gamma - k_z v_z)^2$, it can be shown that the Laplace transform of the equations for the amplitudes $E_n(z) \sim A_n(z) \exp[ik_{zn} z + \delta_n(z)]$ can be expressed approximately in the matrix form [3]

$$\left(s^2 - k_n^2 + \frac{\omega^2}{c^2}\right)\hat{E}_n(s) + \sum_{n'=1}^{N} \frac{\epsilon_{nn'} k_{n'}^2 (\omega^2 + c^2 s^2)}{(\omega - \Omega_c/\gamma + iv_z s)^2} \hat{E}_{n'}(s)$$

$$= sE_n(0) + \sum_{n'=1}^{N} \frac{i\epsilon_{nn'} k_{n'}^2 v_z \omega}{(\omega - \Omega_c/\gamma + iv_z s)^2} E_{n'}(0) , \qquad (7)$$

where use has been made of initial condition $dE_n(0)/dz = 0$, and the dimensionless coupling constants $\epsilon_{nn'}$ are defined by

$$\epsilon_{nn'} = \frac{4\beta_\perp^2}{\gamma \beta_z} \left(\frac{I_b}{I_A}\right) \frac{X_n(r_L, r_g) X_{n'}(r_L, r_g)}{[(\nu_n^2 - 1)(\nu_{n'}^2 - 1)]^{1/2} J_1(\nu_n) J_1(\nu_{n'})} . \qquad (8)$$

In Eqs. (7) and (8), $s = ik_z$ is the argument in the Laplace transform; $\beta_z = v_z/c$ and $\beta_\perp = v_\perp/c$ are, respectively, the normalized axial and transverse velocities of the equilibrium beam electrons; and ck_N is the largest cut-off frequency below the operating frequency ω. Therefore, the amplitudes and dispersion relation can be obtained by solving Eq. (7) and performing the inverse Laplace transform of $\hat{E}_n(s)$.

For two coupled modes, TE_{1n} and $TE_{1n'}$, it is readily shown from Eq. (7) that the dispersion relation is

$$\left(k_z^2 + k_n^2 - \frac{\omega^2}{c^2}\right)\left(k_z^2 + k_{n'}^2 - \frac{\omega^2}{c^2}\right)\left(\omega - \frac{\Omega_c}{\gamma} - k_z v_z\right)^2$$

$$= \left[\epsilon_{nn} k_n^2 \left(k_z^2 + k_{n'}^2 - \frac{\omega^2}{c^2}\right) + \epsilon_{n'n'} k_{n'}^2 \left(k_z^2 + k_n^2 - \frac{\omega^2}{c^2}\right)\right](\omega^2 - c^2 k_z^2) . \qquad (9)$$

When the two modes are well separated, and $\epsilon_{nn} k_n^2(k_z^2 + k_{n'}^2 - \omega^2/c^2) \gg \epsilon_{n'n'} k_{n'}^2(k_z^2 + k_n^2 - \omega^2/c^2)$, corresponding to the electron beam mode, $\omega = k_z v_z + \Omega_c/\gamma$, in resonance with the TE_{1n} mode, $\omega = c(k_z^2 + k_n^2)^{1/2}$, the coupled-mode dispersion relation in Eq. (9) becomes the usual single-mode dispersion relation [2,4]

$$k_z^2 + k_n^2 - \frac{\omega^2}{c^2} = \frac{\epsilon_{nn} k_n^2(\omega^2 - c^2 k_z^2)}{(\omega - \Omega_c/\gamma - k_z v_z)^2} \qquad (10)$$

for the TE_{1n} mode.

Typical results from the computer simulations and kinetic theory are summarized in Figs. 1-3. Figure 1 shows the dependence of rf power in the TE_{11} and TE_{12} modes on the interaction length, for (a) single-mode CARM interactions and (b) the CARM interaction with the two modes coupling to the beam. The system parameters in Fig. 1 correspond to the TE_{11} mode in resonance, and the TE_{12} mode off resonance, with the electron beam. The solid curves are the simulation results obtained by integrating numerically Eqs. (1)-(4), and the dashed curves are obtained analytically from Eq. (7). The inclusion of the coupling of the TE_{11} and TE_{12} modes results in instability for the TE_{12} mode in Fig. 1(b), while the single-mode theory predicts complete stability for the TE_{12} mode in Fig. 1(a). In fact, in Fig. 1(b), the TE_{12} mode grows parasitically with the dominant unstable TE_{11} mode and the two coupled modes have the same spatial growth rate $-\text{Im}\Delta k_z > 0$, corresponding to the most unstable solution of the dispersion relation in Eq. (9). Because the TE_{11} mode is in resonance with the beam mode and the TE_{12} mode is detuned from the corresponding resonance, the TE_{12} mode suffers greater launching losses than the TE_{11} mode in the interaction. This is one of the general features of the multimode CARM interaction, namely, all of the coupled modes have the same small-signal growth rate but suffer different launching losses depending upon detuning characteristics.

Another interesting feature of the multimode CARM interaction is that the rf power distribution among the coupled modes at saturation is *insensitive* to the power distribution at $z = 0$ but is *sensitive* to detuning. Figure 2 shows the results of the simulations for the coupling of the TE_{11} and TE_{12} modes with two different distributions of input rf power. Here, only the TE_{12} mode is plotted because the TE_{11} mode remains virtually unchanged for the two cases. Figure 3 depicts the detuning characteristics of saturation rf power distribution over four coupled TE_{1n} modes ($n = 1, 2, 3, 4$), as obtained from the simulations with an input power of 100 W per mode. By increasing the axial magnetic field B_0 in Fig. 3, the beam mode is tuned through the resonances with the TE_{11}, TE_{12}, TE_{13}, and TE_{14} modes at $B_0 = 3.74$, 4.29, 5.33, and 6.98 kG, respectively. The fractional rf power for a given mode reaches a maximum at its resonant magnetic field, while the rf power decreases rapidly for off-resonance modes. In the transition from one resonance to another, however, two adjacent competing modes close to the resonance can have comparable rf power levels at saturation.

3. SIMULATIONS OF CARM ABSOLUTE INSTABILITY

Most designs of CARM amplifiers, including our design in Sec. 5, rely on linear theory to determine parameter regimes where the absolute instability [5,6] is below threshold. The theoretcial models used in the calculation of the threshold current assume that

there is no input signal at the drive frequency and that the system in infinite in the axial direction. Both these conditions are, obviously, violated in any amplifier experiment. In order to investigate the possibility of suppressing the absolute instability by injecting a large input signal, the MAGIC particle-in-cell code [7] is being used simulate a CARM amplifier. Parameters have been choosen so that, in the absence of an injected signal, the absolute instability will experience strong growth. At present, the cylindrically symmetric version of the program is being employed, limiting this preliminary analysis to TE_{0n} waveguide modes.

The growth of the TE_{01} mode downshifted convective instability and absolute instability from numerical noise (with no driver) is illustrated in Figs. 4(a) and 4(b). System parameters are waveguide radius = 1.5 cm, hollow beam radius = 0.75 cm, gamma = 2.967, beam current = 50A, applied longitudinal magnetic field = 13.75 kG, and $\beta_\perp/\beta_\parallel = 1.0$. Figure 4(a) shows E_θ vs. z at $t = 3.6$ nsec. The long-wavelength oscillation of E_θ corresponds to the convective downshifted guide wavelength of 28 cm predicted by linear theory. Figure 4(b) shows the same field at $t = 8.1$ nsec. The long wavelength is now consistent with the absolute instability guide wavelength of 18cm predicted by linear theory. Apparently, the growth of the downshifted convective instability has been suppressed by that of the slower growing absolute instability.

To illustrate the effects of an input signal, we apply a driver of 25 kW to a highly unstable system with the same waveguide dimensions and beam energy as in Fig. 4, but with $\beta_\perp/\beta_\parallel = 1.6$, beam current = 500 A, and an applied longitudinal magnetic field of 19.43 kG. The frequency of the driver is 34.272 GHz (equal to that of the upshifted intersection of the uncoupled beam and TE_{01} waveguide dispersion relations). At early times growth is predominately in the upshifted TE_{01} mode. It is evident from Fig. 5, where E_θ vs. z is plotted at a time of $t = 1.4$ nsec, that an instability of a longer wavelength, equal to that of either the TE_{01} downshifted ($\lambda_g = 3.9$ cm) or absolute instabilities ($\lambda_g = 3.8$ cm), has developed in the region $z \leq 0.16$ m. If the power of the driver is increased to 2.5 MW, then, as is evident from Fig. 6, no significant longer-wavelength growth has appeared within 3.6 nsec. Further theoretical and numerical studies will be needed to quantitatively understand this phenomena and to determine if it is advantageous for CARM amplifiers to operate in this regime.

4. CARM AMPLIFIER PHASE STABILITY

An analysis of the phase stability of CARM amplifiers to perturbations in electron beam parameters has been performed [8]. For a high peak power rf source to be attractive for use in powering the next generation linear collider, the source must produce rf with a stable, non-varying phase. Both the phase stability during the single 50 ns – 1 μs rf pulse, and the shot-to-shot phase stability must meet certain requirements which depend on the

6

particular design of the linear collider. Failure of the source to deliver phase stable rf output usually results in an unacceptable variation of the energy of the electron beam in the linear collider. The rf phase in a high gain amplifier will be sensitive to the variations of the electron beam energy and current during the pulse. The typical phase stability of conventional klystrons is approximately $8°$ per percent beam energy variation.

In the cyclotron autoresonance maser, the question of phase stability is complicated by the fact that the beam transverse momentum $p_\perp$ (or, correspondingly, the transverse velocity $\beta_\perp$) is independently variable from the beam energy. For a free-electron laser, the beam transverse motion is set by the wiggler, such that $\beta_\perp = a_w/\gamma$. The phase stability of the CARM amplifier must therefore be investigated with respect to potential variation in at least three beam parameters, energy γ, transverse momentum $p_\perp$, and current I. These parameters are interrelated. For example, the current is correlated to the voltage fluctuations for space-charge limited emission from the cathode, and the beam $p_\perp$ will be correlated with fluctuations in the beam energy through the wiggler which is employed to produce the $p_\perp$ (assuming that a wiggler is used to spin up the beam).

Phase stability studies for several CARM amplifier designs have been carried out. For the parameters outlined in Table 1, the net rf phase variation with fluctuations in both beam voltage and $\beta_\perp$ is shown in Fig. 7 for energy $E = mc^2(\gamma - 1)$ and $\beta_\perp$, when γ and $\beta_\perp$ are assumed to be independently variable parameters. The contours are straight lines. In these figures, the phase shift between the amplifier input phase and the amplifier output phase has been taken to be zero for the mean values of the design parameters.

In a real CARM amplifier which utilizes a Pierce-Wiggler for the helical beam formation, the wiggler produces a correlation between the beam $\beta_\perp$ and the instantaneous beam energy in the wiggler. This correlation depends on how close the device is operating to resonance between the guide field and the wiggler field, exact resonance at the entrance of the wiggler occurring when $\gamma\beta k_w c = eB_0/m$. By a careful choice of the wiggler and guide field parameters, this wiggler induced correlation between fluctuations in γ and fluctuations in $\beta_\perp$ can be chosen in such a way as to significantly reduce the rf phase fluctuation for variations in the electron beam energy. An example follows. For the parameters in Table 1, for a wiggler designed with $\lambda_w = 15\,\mathrm{cm}$, $B_{0w} = 1.964\,\mathrm{kG}$, a wiggler field strength of $B_w = 35.8\,\mathrm{G}$, and a length of $L_w = 45\,\mathrm{cm}$, the wiggler induced correlation between changes in beam voltage and the resulting change in $\beta_\perp$ is shown in Fig. 7 as the arc intersecting the mean value zero phase shift point of the contour plot. As is apparent from this figure, by careful choice of the wiggler induced correlation between γ and $\beta_\perp$, the rf phase stability of the CARM amplifier can be greatly enhanced. Fig. 8 presents a summary of the phase variability for independent voltage and $\beta_\perp$ variation, and for beam voltage when the beam is intentionally correlated (corrected) by proper design of the wiggler system. Uncorrellated variations are $\pm 8°$ per percent energy variation, $\pm 15°$ per percent variation in $\beta_\perp$, but only $\sim \pm 2°$ per percent variation in beam

energy, over a narrow range of energy change ($\sim \pm 2.5\%$), for the properly designed correlation between $\beta_\perp$ and γ. For large variations in the beam energy, the wiggler induced correlation should result in the expected large variations in amplifier output phase; the wiggler induced correlation will only correct the phase for small changes about the design energy.

This technique for local reduction of the CARM amplifier phase sensitivity to beam energy variations could significantly improve the prospects for a high-gain CARM amplifier with a high degree of phase stability.

5. EXPERIMENTAL DESIGN

Experimental designs for both a long-pulse and short-pulse CARM amplifier have been carried out. The long-pulse experiment will utilize a $0.27\,\mu$P, 700 kV electron gun, and the MIT $2.5\,\mu s$ ($1\,\mu s$ flat-top), 700 kV pulse modulator. For operation with pulse lengths of $1\,\mu s$, the design of the CARM amplifier must optimize the device efficiency within the constraints imposed by the requirement that the amplifier not be susceptible to absolute instabilities [5,6]. Because the $1\,\mu s$ pulse length is significantly longer than the typical e-folding times of the absolute instability, the design parameters of the device must be well within the calculated stability limits.

The beam pitch angle $\alpha \equiv \theta_{p0}$ which corresponds to 50% and 80% of the critical coupling for instability is shown in Fig. 9 as a function of the normalized detuning from resonance Δ for three different beam voltages. This detuning is defined by

$$\Delta \equiv \frac{2\,(1 - \beta_{\|0}/\beta_\phi)}{\beta_{\perp 0}^2\,(1 - \beta_\phi^{-2})}(1 - \frac{\beta_{\|0}}{\beta_\phi} - \frac{\Omega_c}{\gamma\omega}).$$

The total efficiency as a function of detuning, with beam $\alpha \equiv \theta_{p0}$ determined as a function of Δ from Fig. 9, is shown in Fig. 10 for the case of a cold beam. The drive power was $P_d = 1\,$kW, and the guide radius $r_w = 1.11\,$cm for these simulations. Results were obtained from a code which integrates a single mode version of Eqns. (1)–(4). The device efficiency is seen to increase markedly for magnetic fields below resonance; this is primarily because the allowable beam θ_{p0} increases substantially as the magnetic field is lowered. For fixed θ_{p0} the device efficiency does not vary with field as dramatically as in Fig. 10. Amplifier efficiency enhancement has been shown possible with magnetic field tapering [9,10]. The design parameters for a choice of 550 kV as the beam voltage are shown in Table 2.

6. CONCLUSIONS

CARM theory and simulation have been used to study amplifier performance in overmoded systems. A multimode theory, which can predict the transverse mode excitation,

including launching losses, is in good agreement with multiparticle simulations. It was shown analytically, and confirmed in the simulations, that all of the coupled modes grow at the same growth rate as the dominant unstable mode, but suffer different launching losses, which depend upon detuning. The saturated rf power in each mode was found to be insensitive to input rf power distribution, but sensitive to detuning.

The absolute instability can be suppressed with sufficiently large input rf power for beam parameters which would otherwise be absolutely unstable. Further studies of this phenomena are required to determine if high gain and suppression of the absolute instabilty can be achieved simultaneously.

The sensitivity of the CARM induced phase shift in the rf signal to variations in the beam volatage and $\beta_\perp$ has been examined in detail. When a Pierce wiggler is used to spin-up the beam, the correlations between errors in energy and perpindicular velocity can be made to cancel (to first order) near the operating point. For the design presented in Sec. 4, sensitivities are, assuming no correlations between energy and $\beta_\perp$, $\pm 8°$ per percent energy variation and $\pm 15°$ per percent variation in $\beta_\perp$, but only $\sim \pm 2°$ per percent variation in beam energy, over a narrow range of energy change ($\sim \pm 2.5\%$), when the errors are correlated by the Pierce wiggler. Experimental design has been presented, and the experiments are underway.

ACKNOWLEDGEMENT

References

[1] B.G. Danly, J.S. Wurtele, K.D. Pendergast, and R.J. Temkin. CARM driver for high frequency RF accelerators. In F. Bennett and J. Kopta, editors, *Proceedings of the 1989 Particle Accelerator Conference*, pages 223–225, I.E.E.E., 1989.

[2] A.W. Fliflet. Linear and nonlinear theory of the Doppler shifted cyclotron resonance maser based in TE and TM waveguide modes. *Int. J. Electron.*, 61:1049, 1986.

[3] C. Chen and J.S. Wurtele. Multimode interactions in cyclotron autoresonance maser amplifiers. *Phys. Rev. Lett.*, 1990. Submitted for Publication.

[4] K.R. Chu and A.T. Lin. Gain and bandwidth of the gyro-TWT and CARM amplifiers. *IEEE Trans. Plasma Sci.*, PS-16:90–104, 1988.

[5] Y.Y. Lau, K.R. Chu, L.R. Barnett, and V.L. Granatstein. Gyrotron traveling wave amplifier: I. analysis of oscillations. *Int. J. Infrared and Millimeter Waves*, 2:373–393, 1981.

[6] J.A. Davies. Conditions for absolute instability in cyclotron resonance maser. *Phys. Fluids*, B1:663–669, 1989.

[7] B. Goplin and *et al*. *MAGIC Particle-in-Cell Code Manual*. Mission Research Corporation, Newington, VA.

[8] W.L. Menninger, *et. al*, Phase Stability of CARM Amplifiers, In Preparation, 1990.

[9] K.D. Pendergast, B.G. Danly, R.J. Temkin, and J.S. Wurtele. Self-consistent simulation of cyclotron autoresonance maser amplifiers. *IEEE Trans. Plasma Sci.*, PS-16:122–128, 1988.

[10] C. Chen and J.S. Wurtele. Efficiency enhancement in cyclotron autoresonance maser amplifiers by magnetic field tapering. *Phys. Rev. A*, 40:489, 1989.

Parameter	Value
Energy, $\gamma \, mc^2$	1 MeV
Current, I	3.7 kA
$\theta_{p0} \equiv p_\perp / p_{\parallel}$	0.6
Mode	TE_{11}
Frequency	17.136 GHz
r_w	1.4 cm
Detuning, Δ	0

Table 1: Average Beam Parameters for Phase Stability Study

550 kV CARM Amplifier Design

Parameter	Design Value
Frequency	17.136 GHz
Mode	TE_{11}
Beam Energy	550 keV
Beam Current	110 A
r_w	1.111 cm
β_ϕ	1.127
θ_{p0}	0.59
B_{zo}	3.91 kG
Detuning (Δ)	0.35
P_{in}	1 kW
P_{out}	18.2 MW
$\eta_T, \, (\sigma_{pz} = 0)$	30 %
z_{sat}	0.83 m
Saturated Gain	43 dB

Table 2: Long-Pulse CARM Amplifier Design Parameters
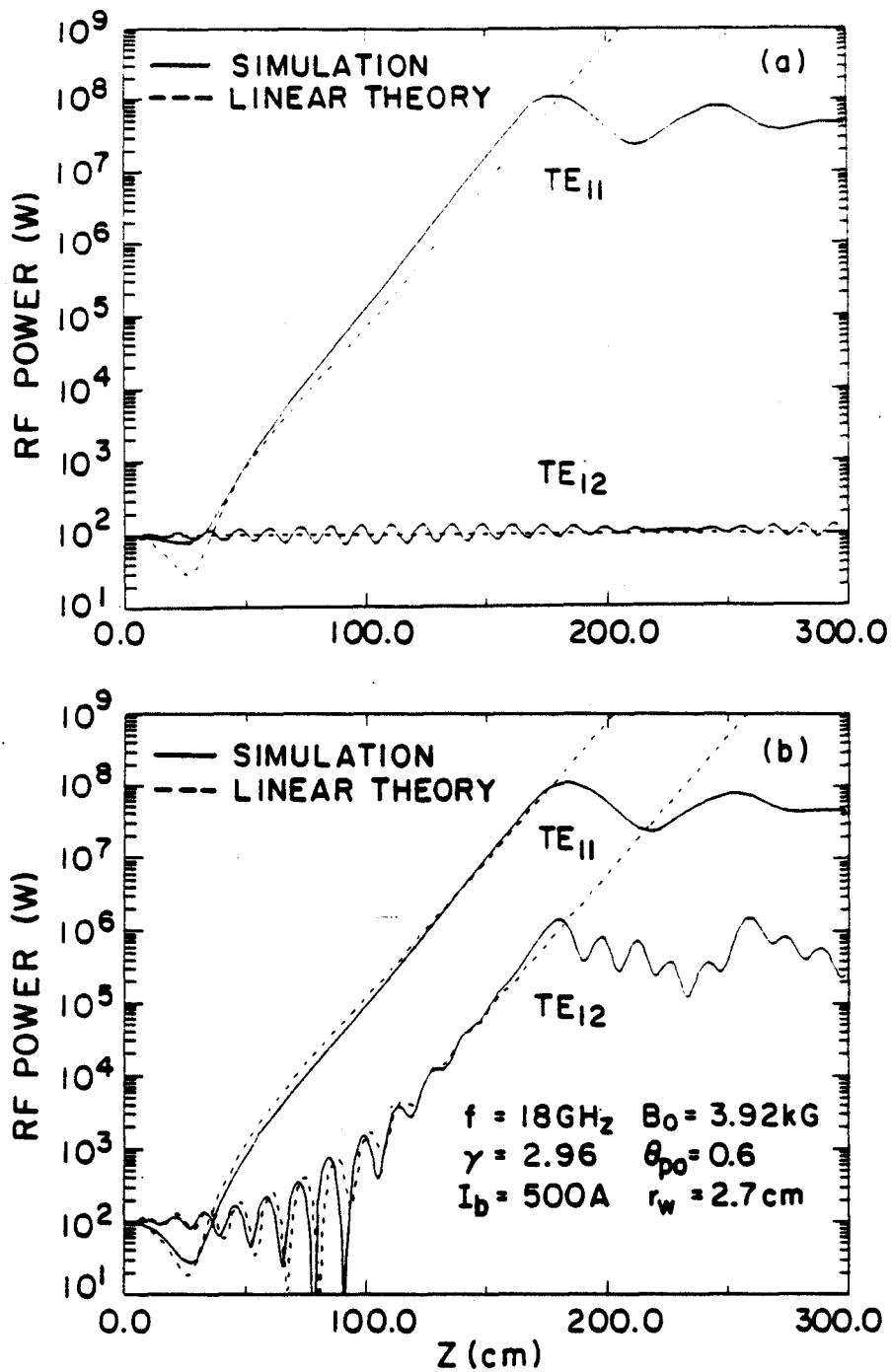
Figure 1: The rf power in the TE_{11} and TE_{12} modes is plotted as a function of the interaction length z for (a) single-mode CARM interactions and (b) the CARM interaction with the two coupled modes. Note in (b) that the TE_{12} mode grows parasitically with the dominant unstable TE_{11} mode at the same spatial growth rate due to mode coupling, despite the differences in launching losses.
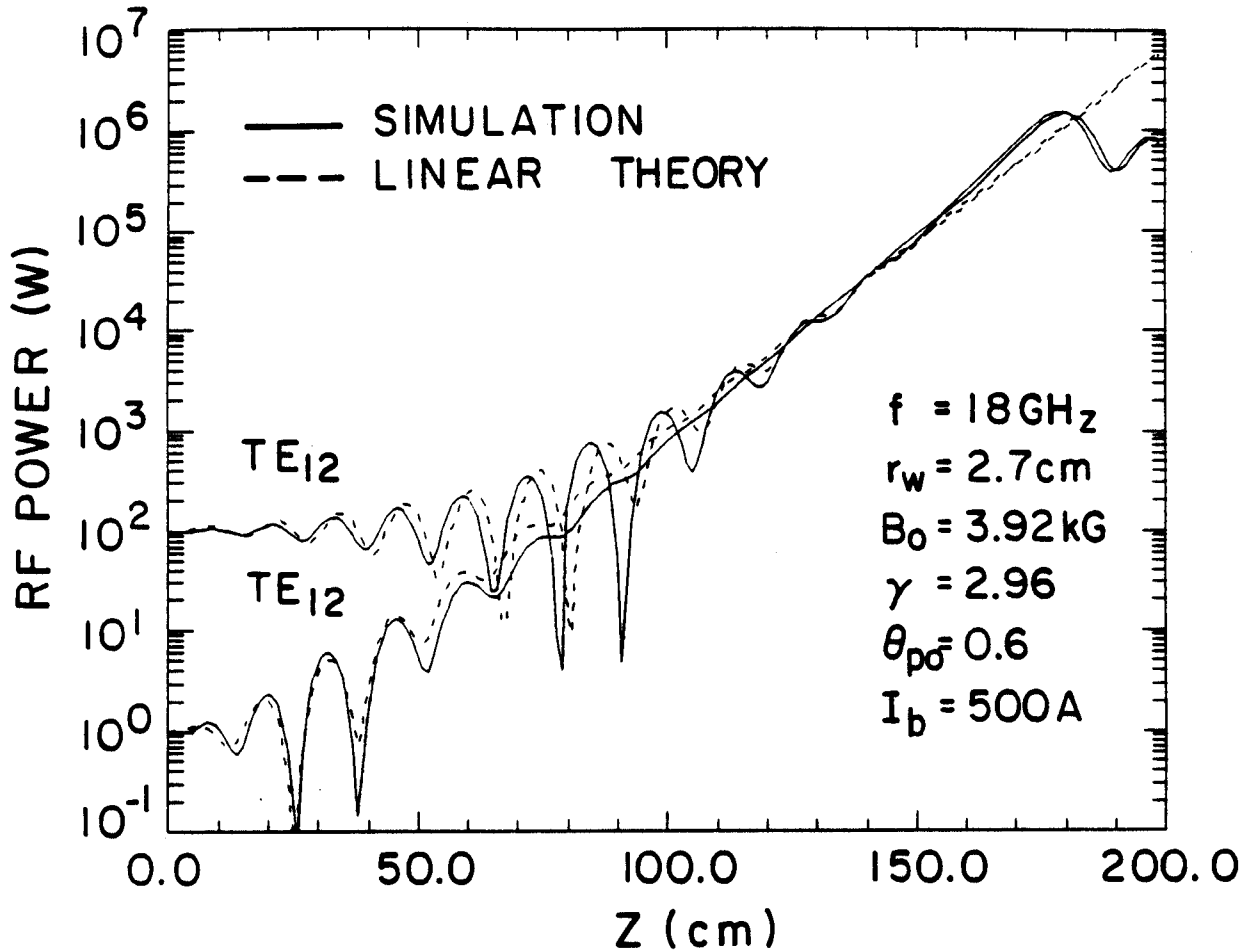
Figure 2: The TE_{12} rf power is plotted as a function of the interaction length for a CARM with the TE_{11} and TE_{12} modes. Here, the two solid curves depict the linear and nonlinear evolution of rf power for the TE_{12} mode obtained from the simulations with two input rf power distributions: (a) $P_0(TE_{11}) = 1.0$ kW and $P_0(TE_{12}) = 1.0$ kW, and (b) $P_0(TE_{11}) = 1.0$ kW and $P_0(TE_{12}) = 1.0$ W, while the two dashed curves are the corresponding analytical results from Eq. (7).
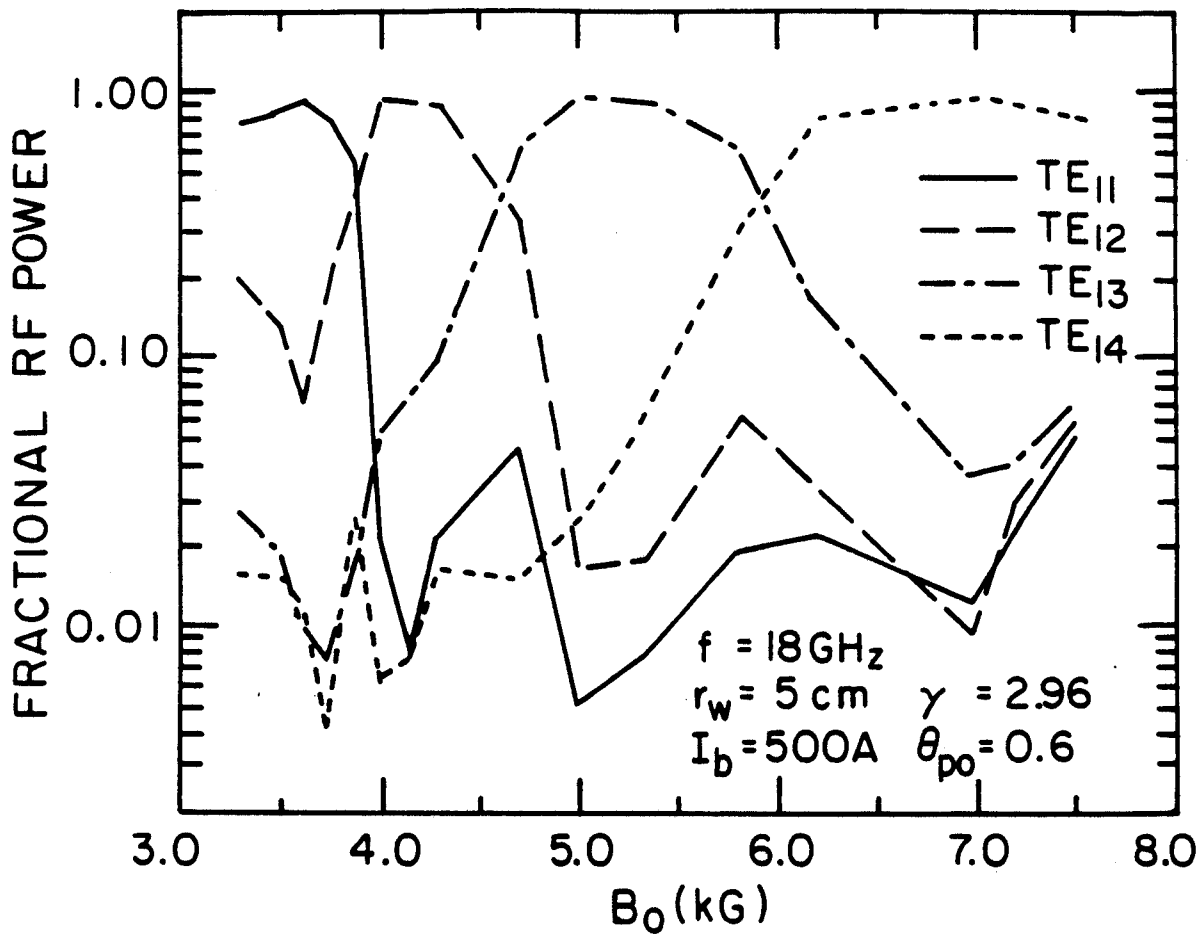
Figure 3: The (fractional) saturated rf power in four coupled TE_{1n} modes is plotted as a function of detuning. Here, the values of the resonating magnetic field for the TE_{11}, TE_{12}, TE_{13}, and TE_{14} modes correspond to $B_0 = 3.74$, 4.29, 5.33, and 6.98 kG, respectively.
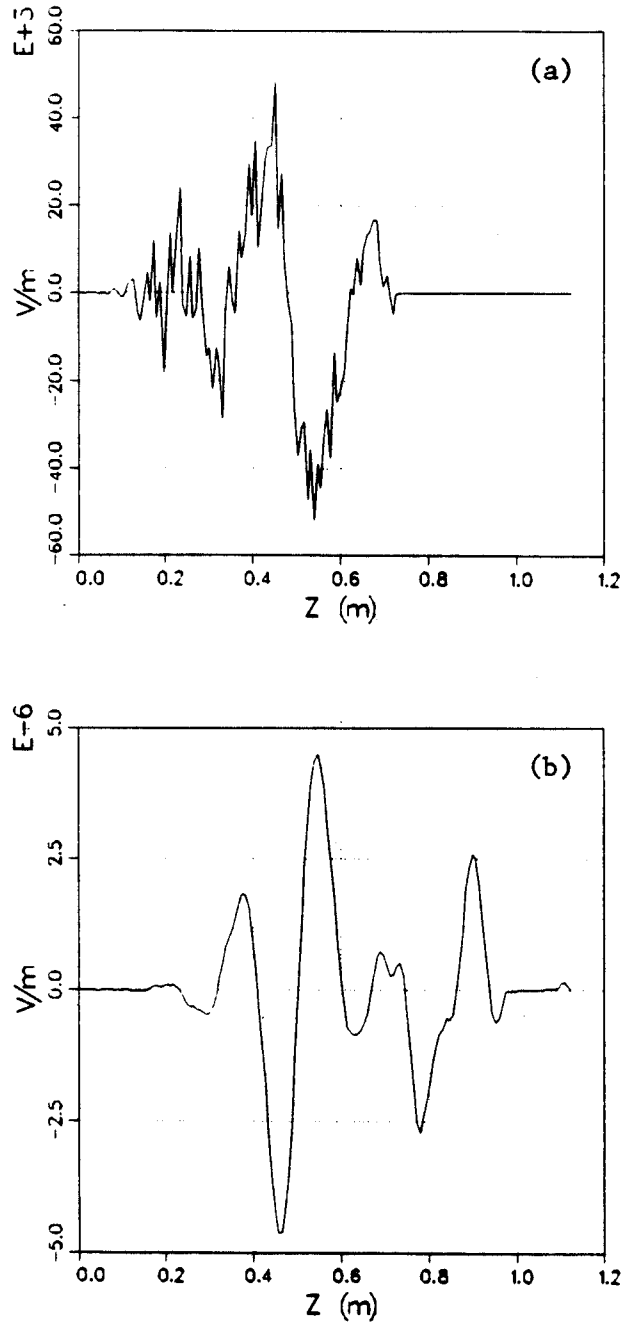
Figure 4: (a) Plot of E_θ vs. z for a CARM with parameters $r_w = 1.5\,\text{cm}$, $R_b = 0.75\,\text{cm}$, $\beta_\perp/\beta_\parallel = 1$, $\gamma = 2.967$, $I_b = 50\,\text{A}$, and an applied field of $B_0 = 1.375\,\text{T}$. This signal has developed from numerical noise and is shown at time 3.6 ns, (b) plot of E_θ vs. z for the same parameters as in (a), but at time 8.1 ns.
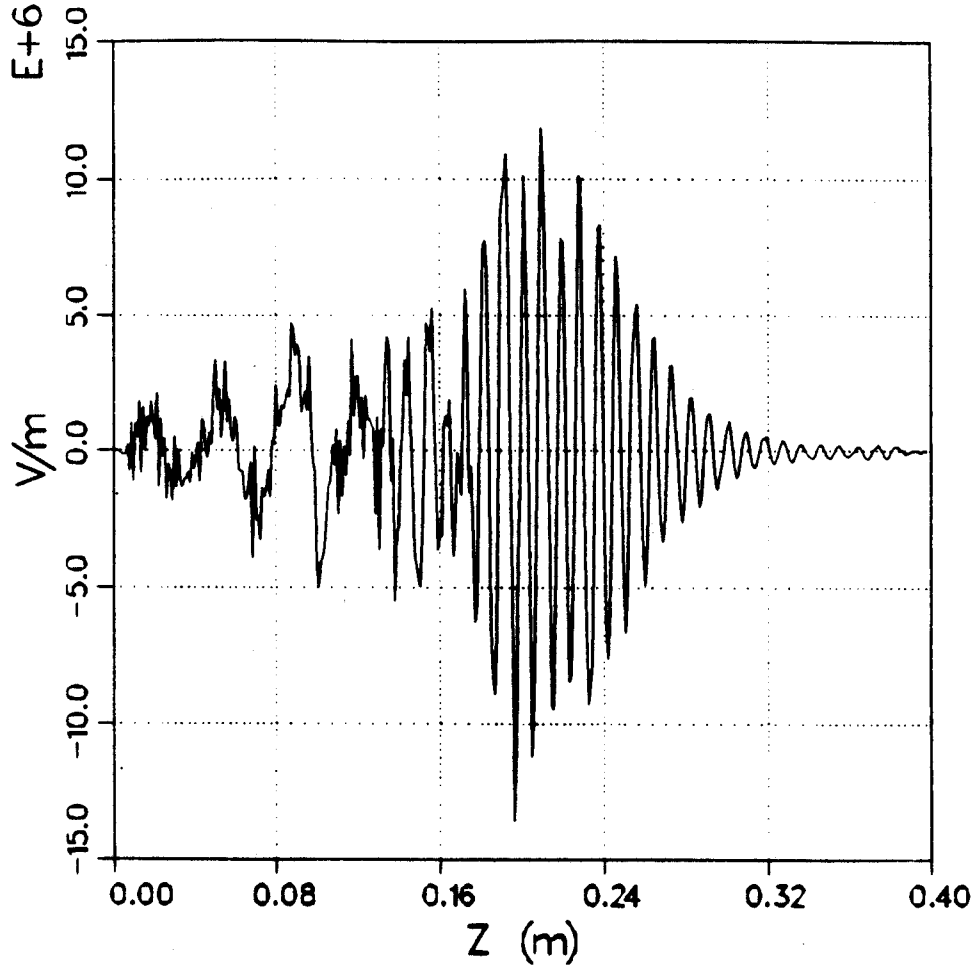
Figure 5: Plot of E_θ vs. z for a CARM with parameters $r_w = 1.5\,\text{cm}$, $R_b = 0.75\,\text{cm}$, $\beta_\perp/\beta_\parallel = 1.6$, $\gamma = 2.967$, $I_b = 500\,\text{A}$, and an applied field of $B_0 = 1.943\,\text{T}$. The driver power is 25 kW. The wavelength to the right of $z = 0.16\,\text{m}$ is that of the driver, the wavelength in the launching loss region (to the left) is either that of the downshifted convective wave or of the absolute instability.
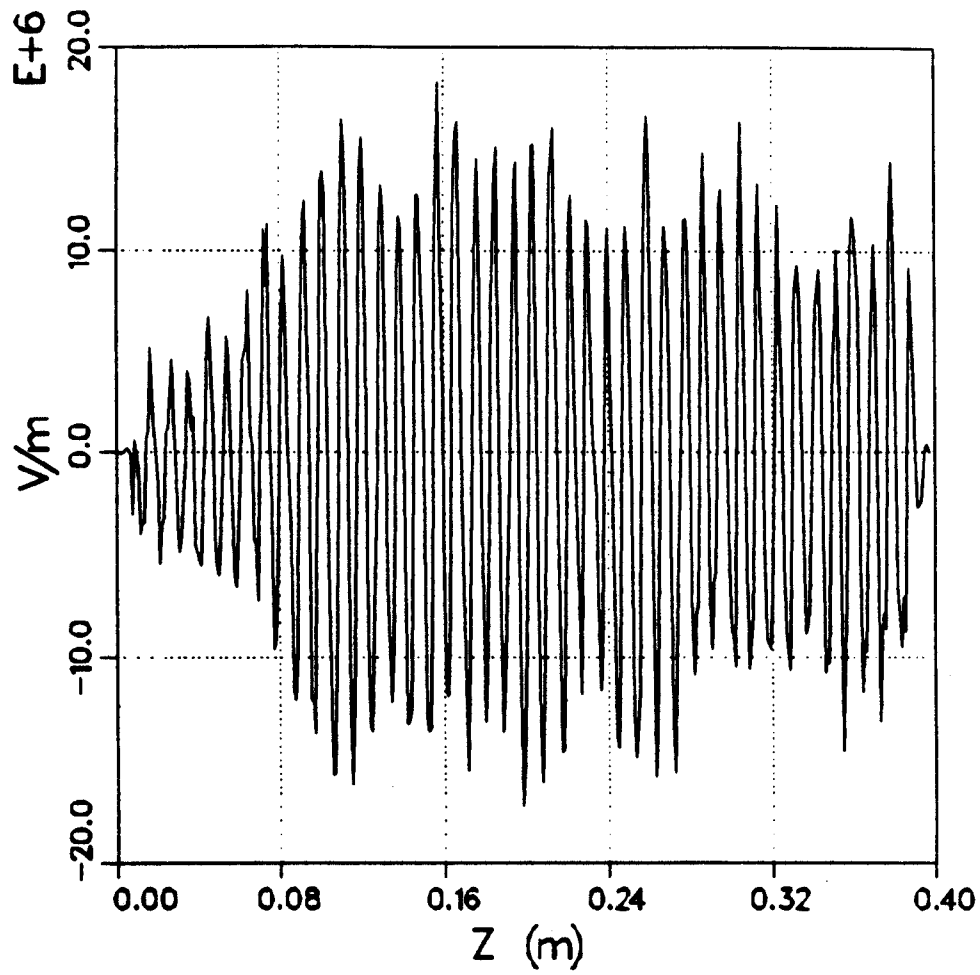
Figure 6: Plot of E_θ vs. z for the same parameters as in Fig. 5, except that the driver power is now 2.5 MW.
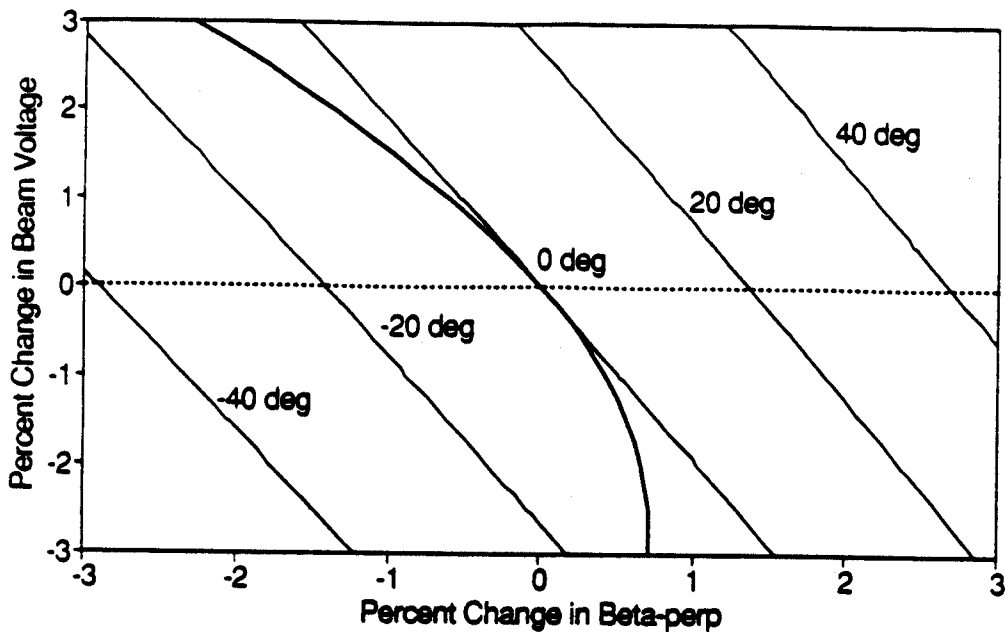
Figure 7: RF Phase Variation Contours in Energy - $\beta_\perp$ Plane. Straight line contours are phase variations for uncorrelated $\beta_\perp$ and voltage V; the curved line represents the correlation between $\beta_\perp$ and V introduced by the wiggler.
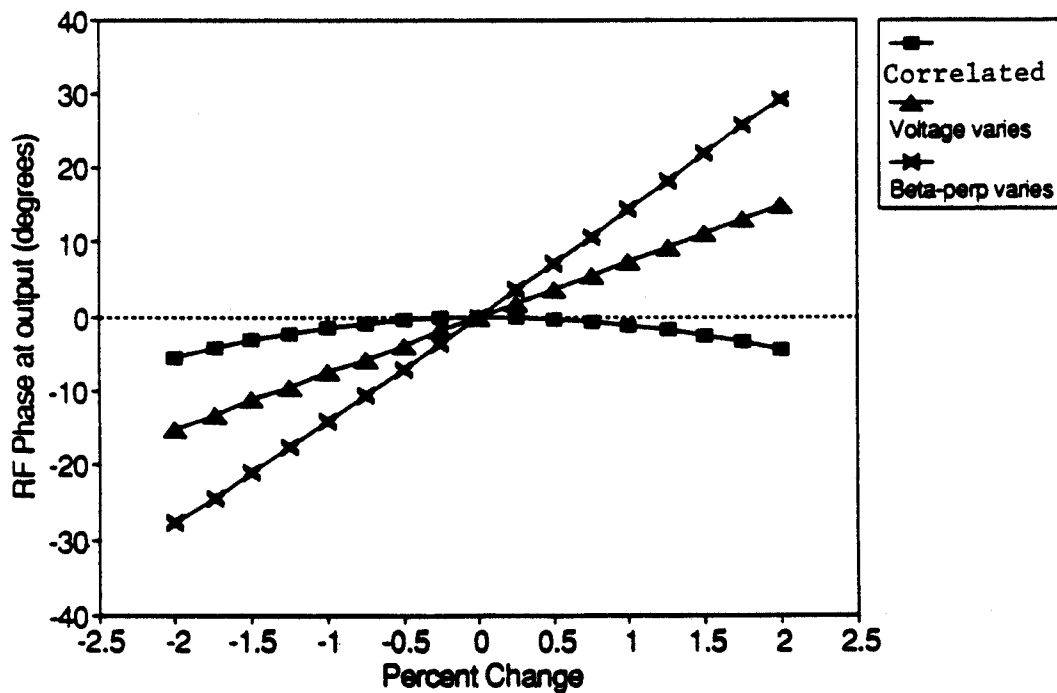

Figure 8: CARM Amplifier Phase Stability for Uncorrelated Energy and $\beta_\perp$ Variation and for Wiggler-Correlated Beam
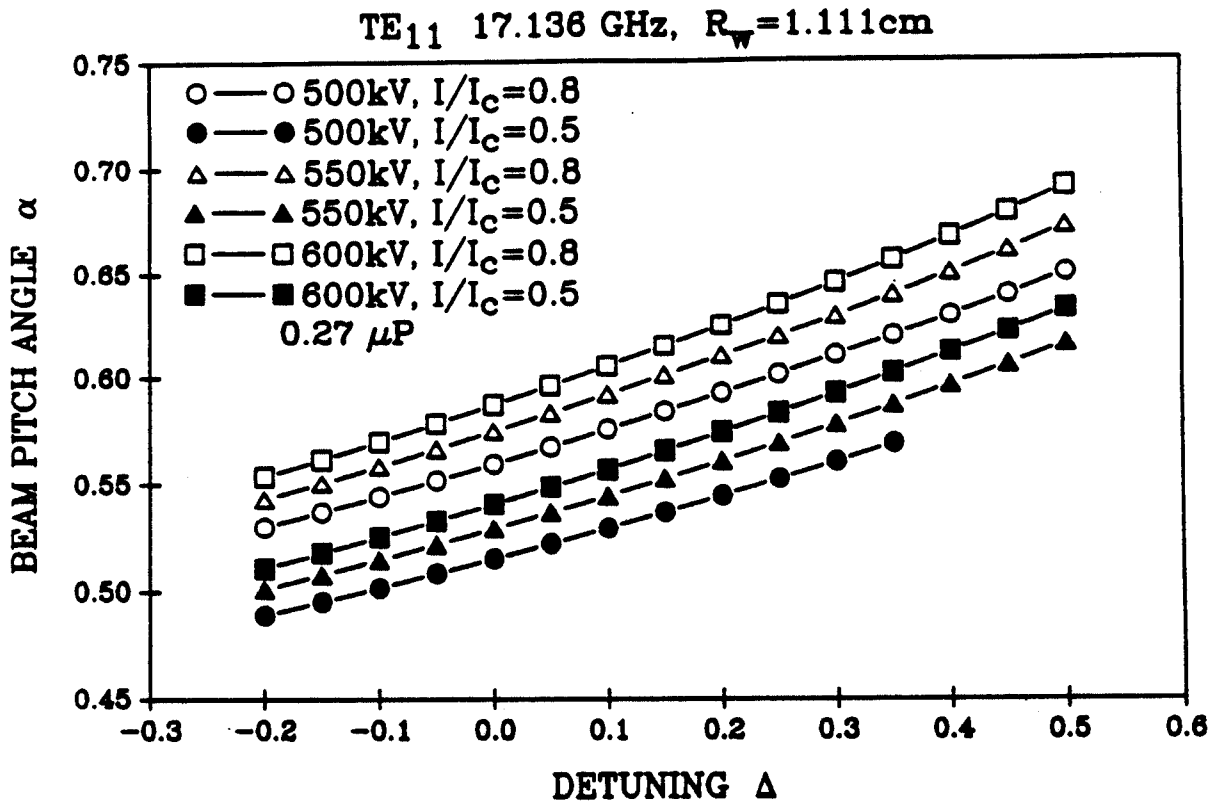
18

Figure 9: Plot of amplifier beam pitch θ_{p0}, corresponding to 50% and 80% of critical coupling as a function of magnetic field, and parametrized by beam voltage, for fixed perveance.
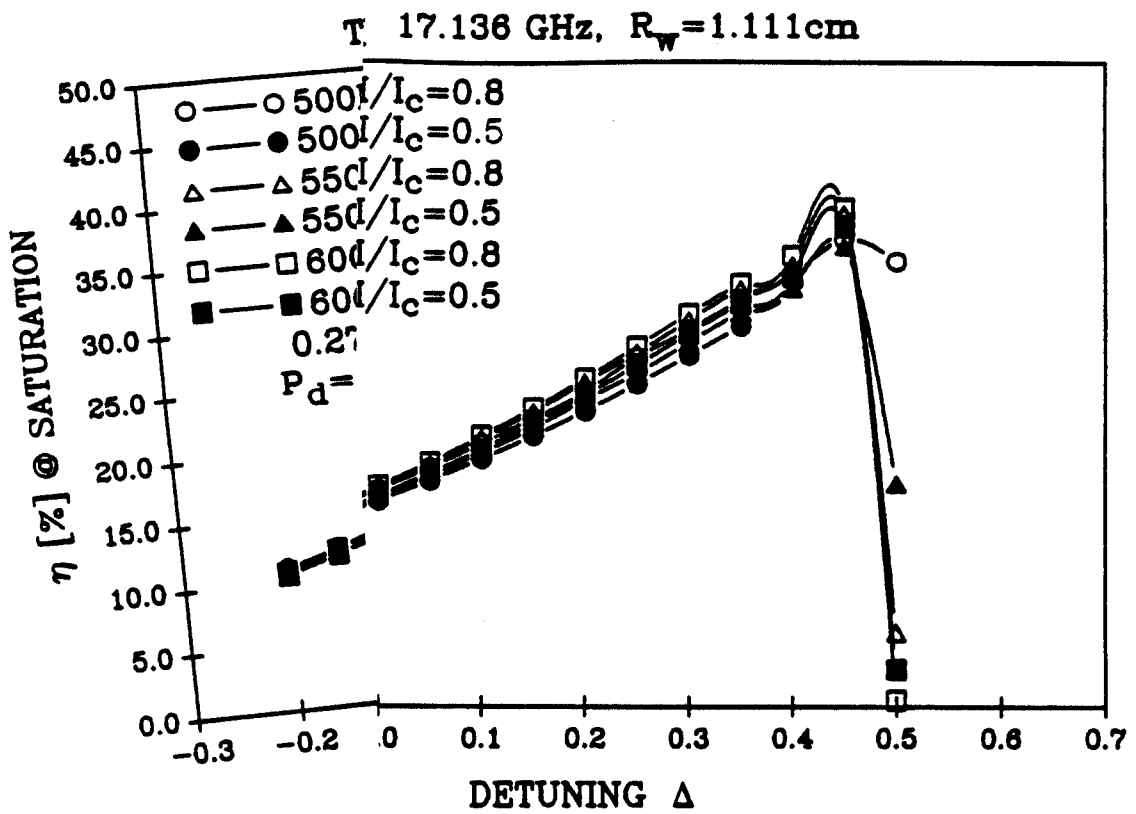
Figure 10: Plot of effi₃ detuning for different beam voltages and for θ_{p0} values corresponding to 50% critical coupling.